Role of internal oceanic variability in the generation of South Indian Ocean Dipole

S. Anjana[1,2], Abhisek Chatterjee[1] and Prerna Singh[1,3]

[1]Indian National Centre for Ocean Information Services, Ministry of Earth Sciences, Hyderabad, India.

[2] School of Ocean Science and Technology, Kerala University of Fisheries and Ocean Studies, Kochi, Kerala, India.

[3]Department of Geophysics, Banaras Hindu University, Varanasi, India.

Corresponding author: Abhisek Chatterjee (abhisek.c@incois.gov.in)

Key Points:

- Internal variability of the Indian Ocean is investigated using a high-resolution eddy-permitting global ocean general circulation model.
- Oceanic internal variability is one of the dominant mechanisms of the interannual variability of the south tropical Indian Ocean.
- The zonal extent of the basin determines the preferential frequency of the variability driven by the internal oceanic instability of the ocean.

Abstract

Interannual/decadal variability in the sea surface temperature at the south subtropical Indian Ocean plays a crucial modulator in the regional climate. The south Indian Ocean dipole mode is one of the dominant modes of such variability. Using a high-resolution global model simulation, we show that internal oceanic variability is one of the primary causes of this observed low-frequency variability in this region. The instability embedded into the large-scale Rossby waves propagates across the south subtropical Indian Ocean, modulating the position and strength of the South Equatorial Current and the South Indian Counter Current. In the process, these current systems impact the thermocline, sea surface height, and the surface temperature of this basin. We further show that the preferential frequency of variability driven by these internal oceanic variabilities is determined by the time these embedded instabilities in large-scale Rosby waves take to cross the longitudinal extent of the south tropical basin.

Plain Language Summary

Variability in the ocean plays an important role in modulating the oceanic conditions, local air-sea interactions, and the regional climate for a longer time scale. The Subtropical Indian Ocean Dipole (SIOD) is the dominant mode of interannual variability in this region and has large impacts on the regional climate. While the atmospheric anomaly is believed to excite an SIOD event, the role of internal oceanic variability in modulating this climate mode was never explored. In some of the previous studies, ocean models were used to understand the impact of internal variability in the Indian Ocean but are mostly limited to the tropical basin due to the model's regional setup. Here, we have used a high-resolution eddy-permitting global model to understand the impact of internal variability in modulating the interannual/near-decadal variability in the Indian Ocean, particularly for the southern tropical Indian Ocean basin. We show that internal variability modulates the meridional migration of South Equatorial Current and South Indian Counter Current leading to low-frequency variability in the sea surface temperature, sea surface height, and the thermocline depth of this basin. Our results highlight that the internal variability is one of the critical parameters to consider for this region's interannual/decadal prediction system.

1 Introduction

Subtropical Indian Ocean dipole (SIOD) is one of the dominant climate modes of interannual variability associated with large-scale sea surface temperature anomaly and wind anomaly in the southern Indian Ocean (SIO; Equator-50^{o}S). The positive phase of SIOD is characterized by a warm SST anomaly in the western Indian Ocean southeast of Madagascar and a cold SST anomaly in the southeast Indian Ocean off the northwestern coast of Australia (Behera & Yamagata, 2001; hereafter referred to as BY01). The second mode of EOF analysis for the interannual SST anomaly, based on Hadley Centre Global Sea Ice and Sea Surface Temperature (HadISST v1; Rayner et al., 2003), depicts the SIOD pattern explaining 13% of the observed interannual variability (Figure 1). Although SIOD is an interannual variability, its evolution is phased locked to the seasonal cycle, which usually develops during October-December, mature in Austral summer, and decays by May-June (Behera & Yamagata, 2001; Suzuki et al., 2004; Zhang et al., 2019). The impact of SIOD is widespread and plays a significant role in modulating regional climate. Its positive phase contributes to the enhanced rainfall in southeastern Africa (BY01; Reason, 2001) and dry year in southwestern Australia (England et al., 2006). This warm SST anomaly off Madagascar also influences the tracks of tropical cyclones in this SIO (Ash & Matyas, 2012) and modules the biogeochemistry with enhanced sea-to-air CO_2 flux of this basin (Zhang et al., 2019). During a positive phase of SIOD, the position of Mascarene high shifts eastward and thus causes weakening of the summer monsoon winds in the early phase of the Indian summer monsoon. Further, in a recent study, Thompson et al. (2016) show that the phase of SIOD influences the cross-equatorial flow of heat content as well by modulating the wind stress curl associated with the Mascarene high and impact the north Indian Ocean sea-level variability in decadal timescale. Hence, understanding the processes that contribute to the evolution of SIOD is very important for the accurate prediction of regional climate.

The role of atmospheric forcing in the evolution of SIOD is well studied. The Mascarene high strengthens and shifts southeastward during the peak phase of the positive SIOD in Austral summer. This resulted in enhanced southeasterly winds over the eastern edge of the high, causing the east pole of SIOD to cool. On the other hand, reduction in latent heat flux associated with advection of humidity and weaker winds cause warming on the western side (BY01; Chiodi & Harrison, 2007). Few studies have also linked the atmospheric variability of the Southern Ocean to the evolution of the SIOD as it accompanies a similar dipole pattern in the south Atlantic (Fauchereau et al., 2003; Hermes & Reason, 2005). SIODs are also weakly correlated with ENSO, with some of the SIOD events co-occur with the La-Nina (BY01; Zhang et al., 2019). However, strong SIODs are also observed without ENSO, indicating a role of other possible forcings in the evolution and generation of such events.

Here, we investigate the role of internal oceanic variability in generating SIODs in interannual to near-decadal timescale (frequently phrased as low-frequency variability) using a high-resolution global ocean general circulation model. Next, we discuss the model configuration and experiments in Section 2. The results are presented in Section 3, and finally, Section 4 concludes our findings.

2 Ocean model and experiments

This study uses a global ocean general circulation model based on Modular Ocean Model (MOM version 5; Griffies, 2012). It uses a global tripolar grid (Murray 1996), with model equations discretized using Arakawa-B staggered gridding and assumes hydrostatic and Boussinesq approximations. The model's horizontal resolution is eddy-permitting and is set to $1/8^{o}$, i.e., ~13.75 km at the equator. In the vertical, it uses 42 z-star levels with top 22 levels confined within the first 200 m of the water column. Such high horizontal and vertical resolutions allow realistic simulation of eddy activities in the SIO and Antarctic Circumpolar Current (ACC) regime. As we will see in the subsequent sections, this is one of the prerequisites to account for this region's internal variability and, therefore, to simulate SIODs realistically. The bottom topography of the model is derived from a modified ETOPO2 bathymetry dataset (Sindhu et al., 2007). The multi-dimensional, piecewise parabolic method (MDPPM) is used for vertical and horizontal advection with a flux limiter based on the MITgcm (Massachusetts Institute of Technology, Cambridge, general circulation model). The vertical mixing scheme is KPP (Large et al., 1994), with the bulk Richardson number set to 0.3. A blend of Laplacian and biharmonic friction has been used for horizontal mixing. The shortwave penetration scheme applied is based on the estimation of chlorophyll-a climatology from SeaWiFS (Manizza et al., 2005).

In order to understand the role of internal variability in the generation of SIOD, the model is first forced by climatological surface atmospheric fluxes from CORE-II climatological forcing (Large & Yeager, 2009). The model is initialized using temperature and salinity from the climatology adopted from Chatterjee et al. (2012) with a state of rest. The climatological simulation is carried out for 175 years, and only the last 50 years of simulation (126-175) are analyzed in the study to avoid the initial spin-up period. Hereafter this climatological model simulation will be referred to as MOMCL. The model is further integrated forward using interannual forcing from JRA55do (Tsujino et al., 2018) for 1958-2017 and is referred to as MOMCR.

Comparison of the first two EOF modes of SST anomaly between observation and MOMCR suggests that the model could faithfully reproduce the variability in the SIO region (Figure 1). The leading mode represents basin-wide warming associated with the El-Nino forcing and is reproduced reasonably well by the model. However, it explains only 20% variability in the model compared to 32% in the observation. On the other hand, the second EOF mode, which represents the SIOD pattern and is of interest in this study, is reproduced quite accurately by the model with a similar spatial pattern and explains comparable variability. Further, the correlation for the second principal component between the model and observation is also very high with a correlation coefficient 0.85. This indicates the realism of the model configuration used in this study.

In the subsequent sections, we will frequently use anomalies of the model simulated variables like SST, sea surface height (SSH), and D20 (depth of the 20°C isotherm; representative of the depth of the thermocline). These anomalies are calculated by removing the averaged annual cycle derived using the last 50 years of MOMCL simulations (126-175th climatological years). Further, the eddy kinetic energy of MOMCL simulation in the low-frequency band is calculated based on anomalies in zonal and meridional velocities.

3 Results

3.1 SIOD and its variability

In the present study, we use the difference of SST anomalies between the western (55°E-65°E, 27°S-37°S) and eastern (90°E-100°E, 18°S-28°S) SIO basin to define the SIOD index following the definition of BY01 (Figure 2a). The choice of this definition is also supported by the very strong correlation (correlation coefficient exceeding 0.9) between the SIOD index and the principal component of the second EOF for HadISST. MOMCR reproduces the SIOD index faithfully with a correlation coefficient of 0.82 (> 95% significance) (Figure 2a). Spectral decomposition of this SIOD index suggests energy peaks in the interannual period of 1.5-4 years and a strong near-decadal period with periodicity in the range of 6-7 years (Figure 2b). For brevity, hereafter, we refer to this inter-annual to near-decadal variability as low-frequency variability. As the index is defined as a difference between the two SIOD poles, spectral analysis are performed separately for the SST anomaly of the western and eastern box (Figure 2c,d). It shows that such low-frequency variability with a similar periodicity exists in the eastern and western box of the SIOD poles. The low-frequency variability in the eastern SIO has been documented earlier and primarily linked to the equatorial winds in the western Pacific driven by the ENSO variability (Feng et al., 2010; Han et al., 2014). However, it is shown that ENSO has minimal influence in the western SIO south of 15°S (Zhang et al., 2019), which is also reflected in the poor correlation between SIOD and ENSO variability. In the following sections, we will discuss the role of internal oceanic variability in this observed low-frequency variability in the Indian Ocean with special emphasize on the western part of the SIO region.

3.2 Internal oceanic variability

In order to understand the role of internal oceanic variability in this low-frequency periodic band, we investigate the low-frequency variability obtained from model simulation forced by the climatological forcing (MOMCL). Considering the fact that the forcing does not have any energy longer than the annual cycle, the low-frequency variability generated by the model is purely attributed to the internal oceanic variability or instability of the system. In a similar study, Jochum and Murtugudde (2005) studied the role of internal variability in the interannual variability of the Indian Ocean using a simpler reduced-gravity model with relatively coarse horizontal resolution (0.25°). However, their model domain was restricted within the Indian

Ocean north of 25^{o}S. Hence, it was lacking proper lateral boundary conditions and was confined within a domain that does not allow a realistic simulation for the SIO region. Moreover, the impact of cross-basin instabilities, which was missing in their study, was severely underestimated for the Indian Ocean.

Figure 3 shows the standard deviation of anomalies of SST, SSH, D20, and eddy kinetic energy (EKE) for the last 50 years of MOMCL (126-175th climatological years). The influence of internal oceanic variability is quite significant in the 15^{o}S-40^{o}S latitude band of the SIO. While all the variables show considerable variability in this latitude band, there are substantial differences in their spatial patterns. While the SST anomaly shows relatively weaker (~0.2^{o}C-0.4^{o}C) and spread over a broader band in the eastern SIO, it is much stronger (more than 0.5^{o}C) and confined within a narrow region in the western SIO. In contrast, the SSH anomaly shows much broader and stronger variability (more than 10 cm) in the west and is limited within the southwestern part of the Australian coast with a much weaker amplitude in the east. The D20 shows a very strong (~100 m) variability over the western part of the SIO that narrows and weakens towards the east. Along with the other variables, EKE also exhibits strong variability in this region and is mainly confined to a narrow band south of Madagascar in the west and offshore of the west coast of Australia in the east. The discrepancy in the variability patterns between SST anomaly and SSH (D20) anomaly is likely due to the shallow thermocline in the east, allowing SST to change with a slight change in the mixed layer. Whereas, in the west, the thermocline is deep due to Mascarene high and thus requires strong undulation in thermocline to impact the overlying SST. This also reflects in the high standard deviation of SST anomaly that co-locates with the high D20 variability in the western SIO region.

To estimate the relative role of internal oceanic variability with the atmospheric forcing in this low-frequency band, Figure 4 shows the ratio of the standard deviation of the anomalies from MOMCL and MOMCR for SST, SSH, and D20. Hence, smaller (larger) values represent weaker (dominating) influence of internal variability than the atmospheric forcing in generating such low-frequency variability in the Indian Ocean. As seen in Figure 3, a similar spatial pattern is evident in the ratios of respective variables. It shows a strong influence of internal variability in the Mascarene high region in this low-frequency variability. The influence is particularly strong for the SSH and D20 anomaly. The large ratio of the EKE between the MOMCL and MOMCR in the southwestern and eastern edge of the Mascarene high indicates that the internal instability causes substantial variability in the strength of the South Equatorial Current (SEC) and the eastward return flow in the south associated with the South Indian Counter Current (SICC). In turn, variability in this anticyclonic flow causes the observed low-frequency variability in the SIO region (Figure 4e, f).

3.3 Dynamics and scale selection

We further investigate the underlying changes in the current system that excite the low-frequency variability in this region (Figure 5). In a climatological timescale (Figure 5a; averaged over 126-175 climatological years), the SEC, which is primarily fed by the Indonesian throughflow, flows westward between 10^{o}S-18^{o}S. SEC flows in a narrow band in the east and turns broader in the west. It finally splits into the northeast and southeast Madagascar currents (NEMC and SEMC) along the east coast of Madagascar. The SEMC splits further at the tip of Madagascar to partially moves towards the East African Coastal currents and a significant portion retroflect to the east to feed the SICC between 26^{o}S-32^{o}S (Menezes et al., 2014; Schott et al., 2009; Stramma & Lutjeharms, 1997) with a core at ~30^{o}S. The estimated transport for the annual climatological scale is ~ 7 Sv at 60^{o}E, which is found to be similar to the estimates by Menezes et al. (2014). A composite map suggests that the entire circulation migrates to the south during the warm events with the core of the SICC lays near 32^{o}S (Figure 5b). As these current systems migrate to the south, favor downwelling in the western box of the SIOD and causing SST to increase and deepen (elevate) the thermocline (SSH) there. On the other hand, during the cooler events the anticyclonic system migrates northward and the core of the SICC moves to ~28^{o}S (Figure 5c). This northward migration and weakening of current shear cause the shoaling of the thermocline and lower SSH in the western box of the SIOD. The zonal currents longitudinally averaged over the extent of the western box of the SIOD clearly show the transition of the westward SEC north of ~25^{o}S and its eastward retroflect in the south between 26^{o}S-32^{o}S (Figure 5d). The transition zone modulates meridionally in a near-decadal period, evident from the northward propagation of the eastward current after removing the seasonal cycle (Figure 5e). Moreover, in the process, the eastward currents in the south also strengthen intermittently (Figure 5e), causing strong downwelling favorable lateral shear between these two current systems.

Next, we try to understand the mechanisms that determine the timescale of 7-10 years for this region's instability-driven variability. Figure 5g,h shows the hovmöller diagrams of sea level anomaly from MOMCL filtered for 1.5-10 years at 20^{o}S and 27^{o}S, respectively. Both the latitude bands show an evident Rossby wave propagation at this low-frequency periodic band with a propagation speed of ~3.8 m/s and ~2.61 m/s at 20^{o}S and 27^{o}S, respectively and therefore, it takes about 7-10 years depends upon the latitude for the signal to reach the coast of Madagascar from the Indonesian throughflow region. These propagation speeds agree well with the theoretical propagation speed of Rossby waves (Figure 5i) at those latitudes given by $\beta c_n^2/f^2$ ($\beta = \partial f/\partial y$, f is Coriolis parameter and c_n is the characteristic speed of the n'th vertical mode). This indicates that the instabilities that are embedded within the largescale Rossby wave propagation from the ITF intrusion region modulate the mean currents of the SEC and SICC regime. This ultimately modulates the shear and intensity of the downwelling favorable anticyclonic flow of this region. As the Rossby waves take about 7-10 years to travel the entire longitudinal extent from the ITF the influence of this instability-driven variability is also synchronized by a similar timescale. As a result, these low-frequency variabilities in the western SIO region cause strong SIOD events driven by the internal instability at these periodic bands.

4 Conclusions

In this study, we investigate the role of oceanic instability in the generation of SIOD events using high–resolution global MOM5 simulations. SIOD index derived from observation and the control run of the model simulation show strong interannual variability with a periodicity of 1.5-4 years and near-decadal periodicity of ~7 years. Our results based on climatological model simulation show a substantial low-frequency variability in interannual to near-decadal timescale in the 15 ^{o}S-40^{o}S latitude band of the SIO. This indicates the influence of internal oceanic variability or internal instabilities on the climate system of this region. However, the influence of instabilities differs considerably in the spatial variability of SST, SSH, and thermocline. The strongest impact of these instabilities on ocean parameters is seen in the western part of the SIO southeast of Madagascar, which is a region of significant climate importance and the west pole of the SIOD.

Our analysis suggests that the anticyclonic current system that forms off the east coast of Madagascar by the westward flowing SEC in the north and the eastward flowing SICC in the south oscillates in north-south direction with a 7-10 year periodicity. These meridional migrations are found to be driven by instabilities embedded within the large-scale Rossby waves that propagate west from the west coast of Sumatra and Australia. As these large-scale Rossby waves take about 7-10 years to cover the longitudinal extent of the basin, the embedded instability modulates the anticyclonic circulation and its meridional migration at the same timescale. This results in a preferential periodicity in the interannual variability of the SIOD events in the SIO.

These results emphasize the importance of internal instability in the regional climate and, therefore, prediction capabilities in interannual to decadal timescale. Hence, considering that the ineternal variability will remain one of the dominating mechanisms in estimating climate change scenarios, the representativeness of the model simulations in simulating internal instabilities will be the key for success in decadal prediction and climate projections for the next few decades.

Acknowledgments

We thank the Director, INCOIS, for providing the necessary support to carry out this research. The model simulations are performed in a high-performance supercomputer facilitated by the Ministry of Earth Science, Government of India. AS acknowledges the support provided by the Department of Science and Technology for the "INSPIRE" fellowship as part of her PhD programme. Hadley Centre Sea Ice and Sea Surface Temperature data set (HadISST) used here are freely available at Met Office Hadley Centre observations datasets via https://www.metoffice.gov.uk/hadobs/hadisst/. All the figures are prepared using Python. This is INCOIS contribution no. XXX.

References

Ash, K. D., & Matyas, C. J. (2012). The influences of ENSO and the subtropical Indian Ocean Dipole on tropical cyclone trajectories in the southwestern Indian Ocean. International Journal of Climatology, 32(1), 41-56.

Behera, S. K., & Yamagata, T. (2001). Subtropical SST dipole events in the southern Indian Ocean. Geophysical Research Letters, 28(2), 327-330.

Chatterjee, A., Shankar, D., Shenoi, S. S. C., Reddy, G. V., Michael, G. S., Ravichandran, M., Gopalakrishna, V. V., E. Pattabhi, R. R., Uday Bhaskar, T. V. S. & Sanjeevan, V. N. (2012). A new atlas of temperature and salinity for the North Indian Ocean. Journal of Earth System Science, 121(3), 559-593.

Chiodi, A. M., & Harrison, D. E. (2007). Mechanisms of summertime subtropical southern Indian Ocean sea surface temperature variability: On the importance of humidity anomalies and the meridional advection of water vapour. Journal of Climate, 20(19), 4835-4852.

England, M. H., Ummenhofer, C. C., & Santoso, A. (2006). Interannual rainfall extremes over southwest Western Australia linked to Indian Ocean climate variability. Journal of Climate, 19(10), 1948-1969.

Fauchereau, N., Trzaska, S., Richard, Y., Roucou, P., & Camberlin, P. (2003). Sea-surface temperature co-variability in the Southern Atlantic and Indian Oceans and its connections with the atmospheric circulation in the Southern Hemisphere. International Journal of Climatology: A Journal of the Royal Meteorological Society, 23(6), 663-677.

Feng, M., McPhaden, M. J., & Lee, T. (2010). Decadal variability of the Pacific subtropical cells and their influence on the southeast Indian Ocean. Geophysical Research Letters, 37(9).

Griffies, S. M. (2012). Elements of the modular ocean model (MOM). GFDL Ocean Group Tech. Rep, 7, 620.

Han, W., Vialard, J., McPhaden, M. J., Lee, T., Masumoto, Y., Feng, M., & De Ruijter, W. P. (2014). Indian Ocean decadal variability: A review. Bulletin of the American Meteorological Society, 95(11), 1679-1703.

Hermes, J. C., & Reason, C. J. C. (2005). Ocean model diagnosis of interannual coevolving SST variability in the South Indian and South Atlantic Oceans. Journal of Climate, 18(15), 2864-2882.

Jochum, M., & Murtugudde, R. (2005). Internal variability of Indian ocean SST. Journal of climate, 18(18), 3726-3738.

Large, W., & Yeager, S. G. (2009). The global climatology of an interannually varying air–sea flux data set. Climate dynamics, 33(2-3), 341-364.

Large, W. G., McWilliams, J. C., & Doney, S. C. (1994). Oceanic vertical mixing: A review and a model with a nonlocal boundary layer parameterization. Reviews of geophysics, 32(4), 363-403.

Manizza, M., Le Quéré, C., Watson, A. J., & Buitenhuis, E. T. (2005). Bio-optical feedbacks among phytoplankton, upper ocean physics and sea-ice in a global model. Geophysical Research Letters, 32(5).

Menezes, V. V., Phillips, H. E., Schiller, A., Bindoff, N. L., Domingues, C. M., & Vianna, M. L. (2014). South Indian Countercurrent and associated fronts. Journal of Geophysical Research: Oceans, 119(10), 6763-6791.

Murray, R. J. (1996). Explicit generation of orthogonal grids for ocean models. Journal of Computational Physics, 126(2), 251-273.

Rayner, N. A. A., Parker, D. E., Horton, E. B., Folland, C. K., Alexander, L. V., Rowell, D. P., Kent, E. C. & Kaplan, A. (2003). Global analyses of sea surface temperature, sea ice, and night marine air temperature since the late nineteenth century. Journal of Geophysical Research: Atmospheres, 108(D14).

Reason, C. J. C. (2001). Subtropical Indian Ocean SST dipole events and southern African rainfall. Geophysical Research Letters, 28(11), 2225-2227.

Schott, F. A., Xie, S. P., & McCreary Jr, J. P. (2009). Indian Ocean circulation and climate variability. Reviews of Geophysics, 47(1).

Sindhu, B., Suresh, I., Unnikrishnan, A. S., Bhatkar, N. V., Neetu, S., & Michael, G. S. (2007). Improved bathymetric datasets for the shallow water regions in the Indian Ocean. Journal of Earth System Science, 116(3), 261-274.

Stramma, L., & Lutjeharms, J. R. (1997). The flow field of the subtropical gyre of the south Indian Ocean. Journal of Geophysical Research: Oceans, 102(C3), 5513-5530.

Suzuki, R., Behera, S. K., Iizuka, S., & Yamagata, T. (2004). Indian Ocean subtropical dipole simulated using a coupled general circulation model. Journal of Geophysical Research: Oceans, 109(C9).

Thompson, P. R., Piecuch, C. G., Merrifield, M. A., McCreary, J. P., & Firing, E. (2016). Forcing of recent decadal variability in the Equatorial and North Indian Ocean. Journal of Geophysical Research: Oceans, 121(9), 6762-6778.

Tsujino, H., Urakawa, S., Nakano, H., Small, R. J., Kim, W. M., Yeager, S. G., et al. (2018). JRA-55 based surface dataset for driving ocean–sea-ice models (JRA55-do). Ocean Modelling, 130, 79-139

Zhang, L., Han, W., Li, Y., & Lovenduski, N. S. (2019). Variability of sea level and upper-ocean heat content in the Indian Ocean: Effects of subtropical Indian Ocean Dipole and ENSO. Journal of Climate, 32(21), 7227-7245.

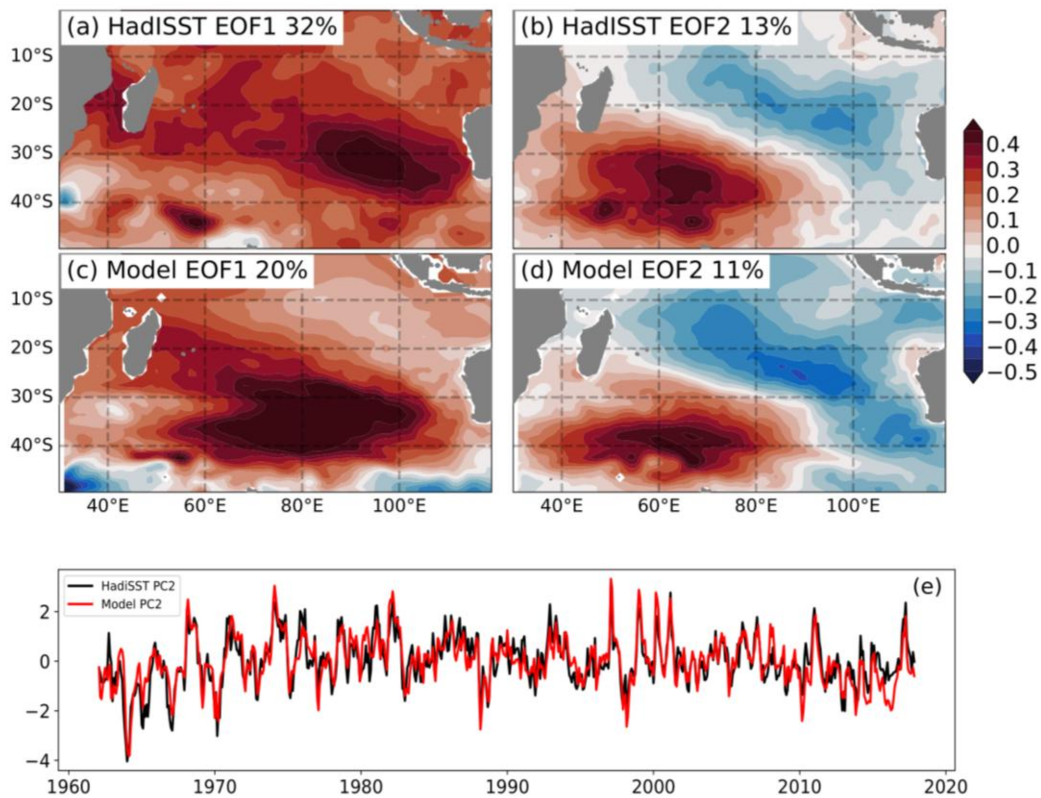

Figure 1. The first and second mode of Empirical Orthogonal Function (EOF) decomposition of SST anomaly of the SIO for the observational HadISST (a,b) and the model simulated SST (c,d). (e) principle component of the second mode of EOF for HadISST (black) and model (red) for 1962–2017.

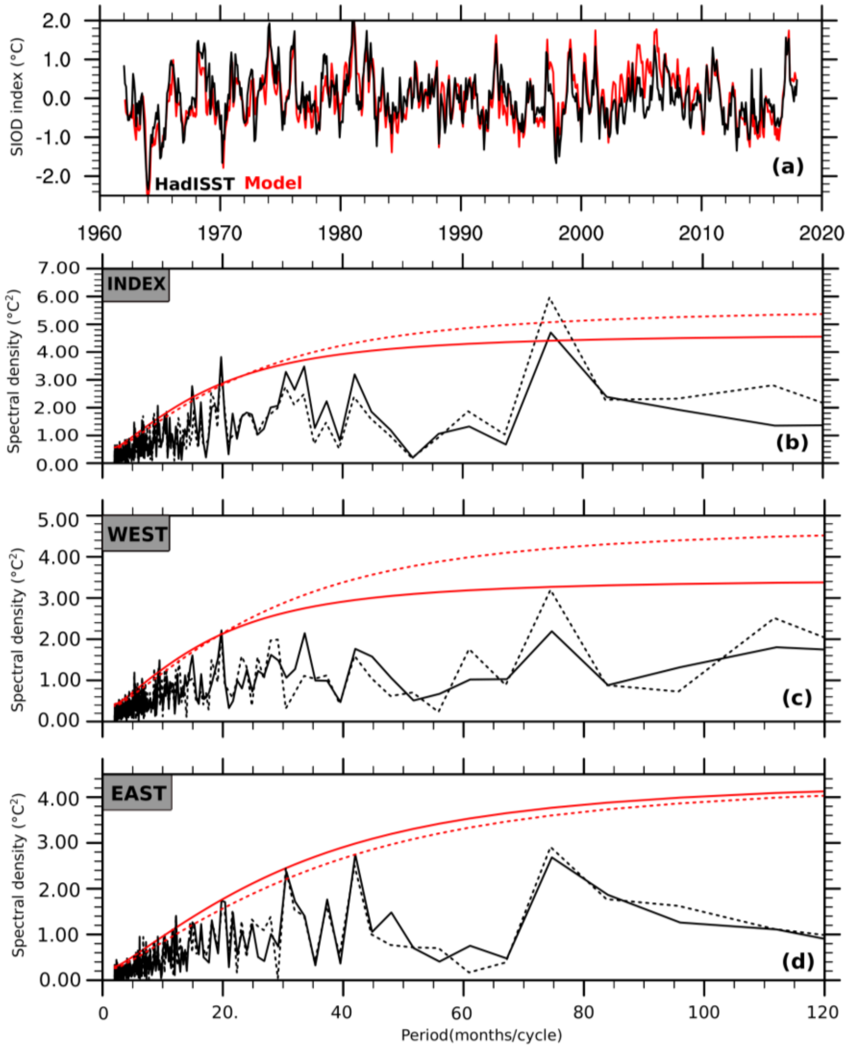

Figure 2. (a) Comparison of SIOD index calculated using HadISST (black) and the model (red) with a correlation coefficient of 0.82. (b) The power spectrum of SIOD index derived from HadISST(solid black) and model (dotted black). (c) Power spectrum of SST anomaly of the western box of SIOD. (d) Same as (c), but for the eastern box of SIOD. The solid (dotted) red line represents 95% significance curve for the spectra derived from HadISST (model).

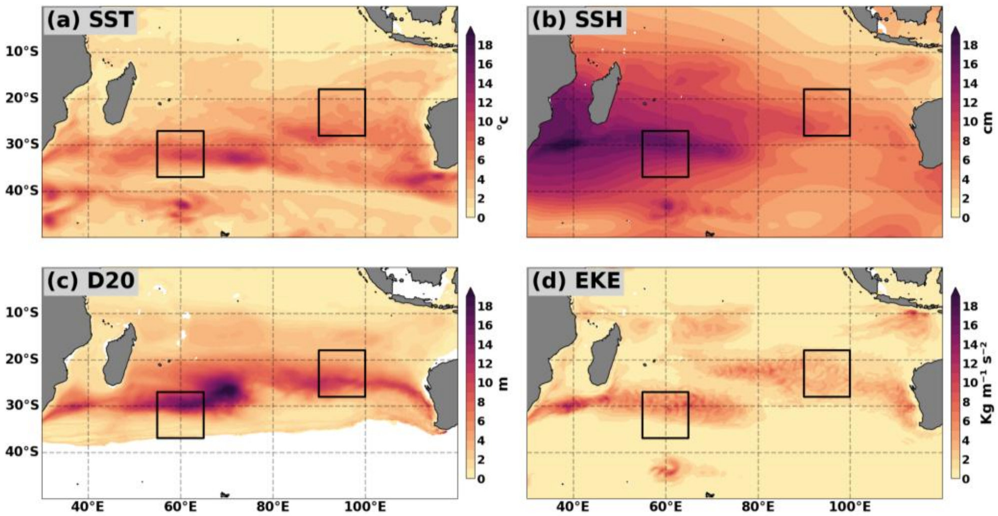

Figure 3. Standard deviation of the model (climatological run) simulated anomalies of (a) SST, (b) SSH, (c) D20, and (d) eddy kinetic energy. The two boxes represent the two poles of the SIOD index.

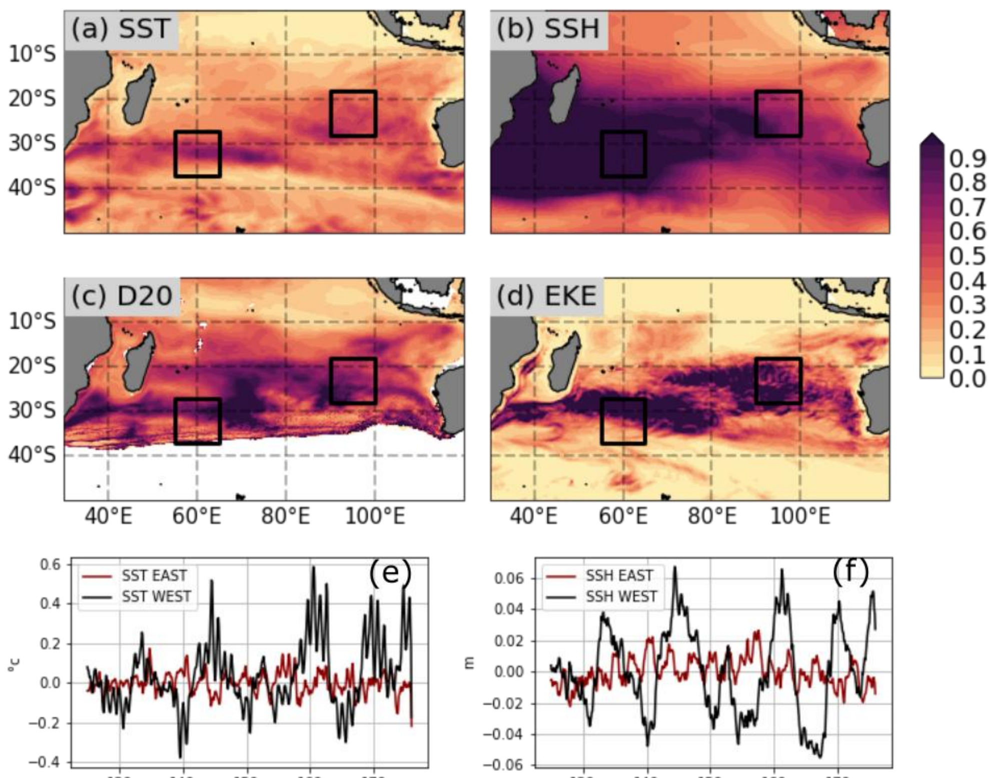

Figure 4. Ratio of the standard deviations of (a) SST, (b) SSH, (c) D20 anomalies, and (d) the eddy kinetic energy derived from MOMCL and MOMCR simulation. The anomalies of (e) SST and (f) SSH averaged over the western (black) and eastern (red) boxes of SIOD.

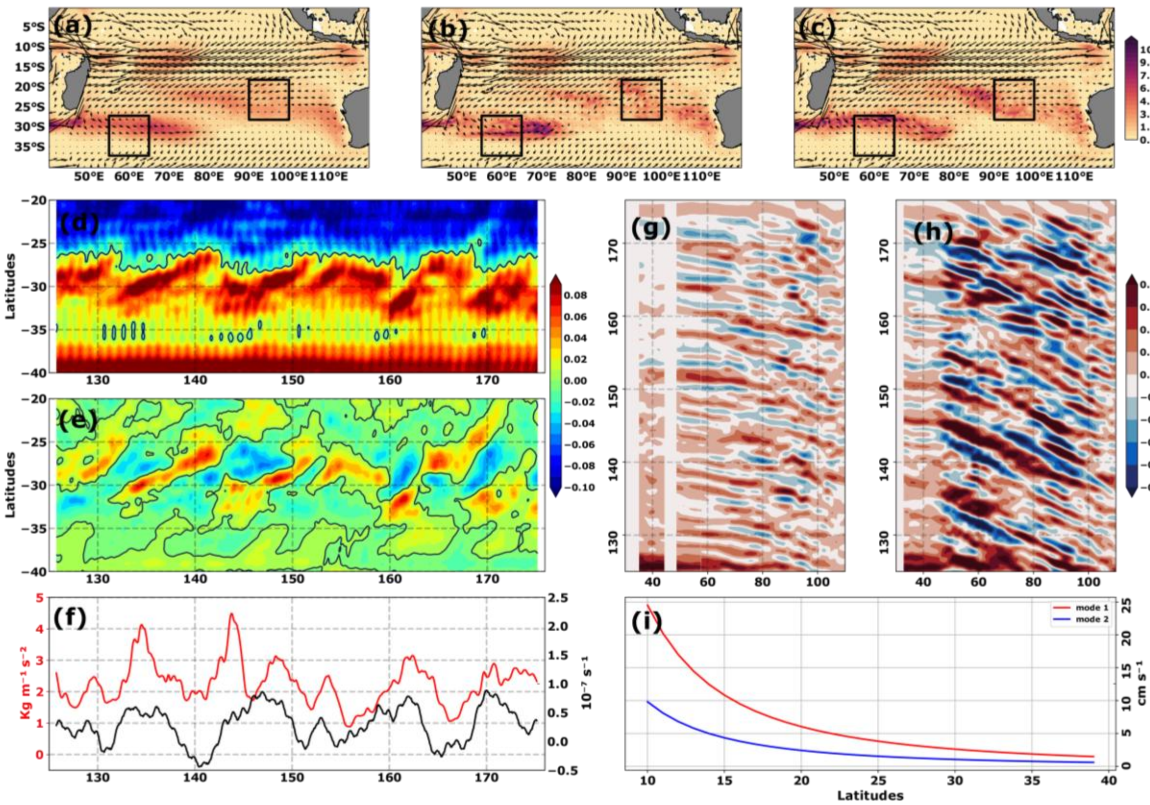

Figure 5. (a) Climatological (averaged over 126-175 simulation years) EKE overlayed by the surface current anomalies. (b) same as (a), but for the composite of warm years (133^{rd}, 147^{th}, 162^{nd}, 171^{st} years; see Figure 4e). (c) same as (a), but for the composite of cold years (131^{st}, 141^{st}, 155^{th}, 166^{th} years; see Figure 4e). Longitudinally averaged (d) zonal current and (e) its anomaly averaged over the west box of SIOD. The black contour represents a zero velocity field. (f) Time-series of EKE (black) and meridional shear in zonal current (dU/dy; red) averaged in the western box of SIOD. Note here that the climatological model simulation years are the x-axis for the panel d,e, and f. Hövmoller diagrams of sea level anomaly from MOMCL band-passed between 1.5-10 years at (g) 20^{o}S and (h) 27^{o}S. (i) Theoretical propagation speed of Rossby waves with respect to latitudes for the first (red) and second modes (blue) in cm/s.